High-Performance Flexible Strain Sensor Fabricated Using Laser Transmission Pyrolysis

Wang, Shaogang; Yang, Huiru; Zong, Qihang; Huang, Qianming; Tan, Chunjian; Gao, Chenshan; Li, Shizhen; Ye, Huaiyu; Zhang, Guoqi; French, Paddy

DOI
10.1109/JSEN.2023.3337233

Publication date
2023

Document Version
Final published version

Published in
IEEE Sensors Journal

High-Performance Flexible Strain Sensor Fabricated Using Laser Transmission Pyrolysis

Shaogang Wang, Huiru Yang, Qihang Zong, Qianming Huang, Chunjian Tan, Chenshan Gao, Shizhen Li, Huaiyu Ye, Guoqi Zhang, *Fellow, IEEE*, and Paddy French, *Fellow, IEEE*

***Abstract*—In recent years, metal crack-based stretchable flexible strain sensors have attracted significant attention in wearable device applications due to their extremely high sensitivity. However, the tradeoff between sensitivity and detection range has been an intractable dilemma, severely limiting their practical applications. Herein, we propose a laser transmission pyrolysis (LTP) technology for fabricating high-performance flexible strain sensors based on (Au) metal cracks with the microchannel array on the polydimethylsiloxane (PDMS) surface. The fabricated flexible strain sensors exhibit high sensitivity [gauge factor (GF) of 2448], wide detection range (59% for tensile strain), precise strain resolution (0.1%), fast response and recovery times (69 and 141 ms), and robust durability (over 3000 cycles). In addition, experiment and simulation results reveal that introducing a microchannel array enables the stress redistribution strategy on the sensor surface, which significantly improves the sensing sensitivity compared to conventional flat surface sensors. Based on the excellent performance, the sensors are applied to detect subtle physiological signals, such as pulse and swallowing, as well as to monitor large-scale motion signals, such as knee flexion and finger bending, demonstrating their potential applications in health monitoring, human–machine interactions, and electronic skin.**

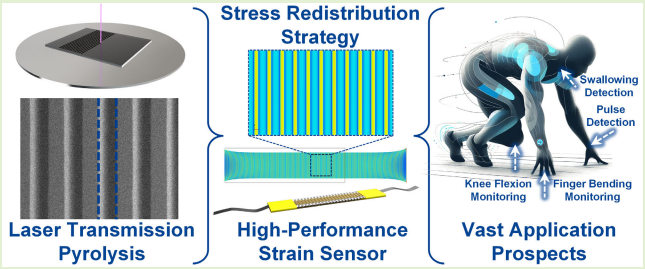

***Index Terms*—Laser transmission pyrolysis (LTP), metal film, polydimethylsiloxane (PDMS) pattering, stretchable strain sensors, ultraviolet (UV) laser.**

I. Introduction

IN RECENT years, the rapid advancement of flexible electronics technology has provided revolutionary impetus to various industries, such as health monitoring [1], human–machine interaction [2], and electronic skin [3]. Flexible strain sensors, as a vital component in the field of flexible electronics, have attracted tremendous attention due to their excellent sensing performance, which includes high sensitivity, wide detection range, fast response time, and robust durability [4]. Generally, according to the signal transmission mechanism, flexible strain sensors can be classified into resistive [5], capacitive [6], piezoelectric [7], and triboelectric [8]. Among these, resistive flexible strain sensors are not only superior to traditional metal conductor [9] and semiconductor [10] sensors in terms of sensing performance but also have the advantages of easy fabrication, low cost, and high plasticity [11], [12]. Typically, resistive strain sensors consist of sensing materials paired with elastic substrates. Conductive materials, such as metal nanomaterials (nanoparticles, nanowires, and nanoplates) [13], [14], [15] and low-dimensional materials (MXene, carbon nanotubes, and graphene) [16], [17], [18], [19], are commonly used as sensing materials for detecting strain changes. Elastic substrates, such as silicone-based substrates [polydimethylsiloxane (PDMS), Ecoflex, and Dagon-skin] [20], [21], [22] and rubber-based substrates (natural rubber, styrene-butadiene rubber, and polyurethane rubber) [23], [24], [25], provide flexibility to sensors and ensure the stability and reliability of the sensing materials.

In terms of the fabrication of strain sensors, the strategies can be categorized into two main types: embedding conductive materials within elastic substrates or attaching conductive materials onto the elastic substrates. The high sensitivity of

Manuscript received 7 October 2023; revised 6 November 2023; accepted 20 November 2023. Date of publication 6 December 2023; date of current version 14 March 2024. The associate editor coordinating the review of this article and approving it for publication was Prof. Guiyun Tian. *(Corresponding author: Shaogang Wang.)*

Shaogang Wang, Chunjian Tan, Guoqi Zhang, and Paddy French are with the Faculty of Electrical Engineering, Mathematics and Computer Science, Delft University of Technology, 2622 CD Delft, The Netherlands (e-mail: S.Wang-10@tudelft.nl; p.j.french@tudelft.nl).

Huiru Yang, Qihang Zong, Qianming Huang, Chenshan Gao, and Shizhen Li are with the School of Microelectronics, Southern University of Science and Technology, Shenzhen 518055, China.

Huaiyu Ye is with the Faculty of Electrical Engineering, Mathematics and Computer Science, Delft University of Technology, 2622 CD Delft, The Netherlands, and also with the School of Microelectronics and the Joint Laboratory for Advanced Situation Awareness, Southern University of Science and Technology, Shenzhen 518055, China (e-mail: yehy@sustech.edu.cn).

Digital Object Identifier 10.1109/JSEN.2023.3337233

strain sensors usually stems from significant structural changes in the material during strain, which leads to drastic changes in conductivity. For example, crack-based strain sensors achieve sensitive strain detection by taking advantage of the formation and expansion of cracks, coupled with their disconnection and reconnection properties. As reported, Kang et al. [26] designed a crack-based resistive sensor composed of platinum (Pt) and polyurethane acrylate (PUA), which exhibited an ultrahigh sensitivity of 2000 over a sensing range of 0%–2%. Subsequently, Lee et al. [27] fabricated a crack-based flexible strain sensor consisting of a gold (Au) layer and polyethylene terephthalate (PET), which demonstrated a sensitivity of about 1600 in a 2% strain field. These pioneering studies proved that introducing cracks into metal film-based strain sensors is an effective strategy to improve their performance. However, due to the tradeoff between sensitivity and detection range, high sensitivity inevitably leads to a narrow detection range, which severely limits the practical application of flexible strain sensors. Therefore, in addition to material innovation, many studies focused on improving the sensing performance of devices by modifying the crack structure [28], such as crack density [29], crack spacing [30], crack depth [31], and crack connectivity [32].

Herein, we have designed and fabricated a flexible strain sensor based on (Au) metal cracks with microchannel arrays to overcome this limitation. To achieve these microchannel arrays rapidly and efficiently, we developed a promising novel technology for patterning the PDMS substrate: the laser transmission pyrolysis (LTP) method. We also summarized the realization conditions and pyrolysis mechanism of the LTP. After the microchannel arrays were fabricated on the PDMS surface, an Au film was deposited using magnetron sputtering to endow resistive properties. Finally, the PDMS substrate with microchannel arrays and an Au film was sliced and packaged into individual flexible strain sensors. By introducing the microchannel array, a stress redistribution strategy was implemented on the PDMS surface, resulting in a significant resistance change in the Au film under the influence of external stress. These flexible strain sensors were characterized by high sensitivity [maximum gauge factor (GF) of 2448], wide detection range (maximum detection range of 59%), precise detection resolution (0.1%), fast response and recovery times (69 and 141 ms), and robust durability (over 3000 cycles). Building on this, we further demonstrated its practical application in detecting both subtle physiological signals (e.g., pulses and swallowing) and large-scale motions (e.g., knee flexion and finger bending).

II. Experimental Section

A. Design and Fabrication

Fig. 1 illustrates the schematic outlining the design and fabrication process for the flexible strain sensors with microchannel arrays using PDMS as a flexible substrate. The process involves six distinct steps. In Step 1, the PDMS elastomer base and curing agent were meticulously mixed in a proportion of 10:1 and degassed. This mixture was poured into a customized acrylic mold with a thickness of 1.0 mm and cured at a temperature of 80 °C for 2 h. In Step 2, the

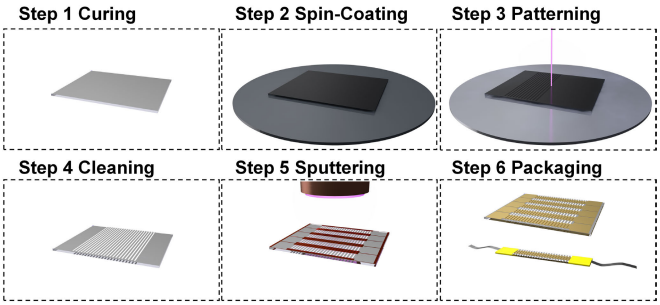

Fig. 1. Schematic illustration of the fabrication process for the flexible strain sensor based on Au microcracks with a microchannel array.

cut rectangular PDMS film (50 × 42 × 1 mm) was attached to a 4-in quartz glass wafer. The film ink was dispersed within a solution containing 10 wt% PVP and ethanol, serving as the light-absorbing material. It was then spin-coated onto the PDMS film at 2000 r/min for 20 s. In Step 3, after the ethanol had evaporated, an ultraviolet (UV) laser was used to perform the LTP reaction on the PDMS substrate with a light-absorbing layer to create a microchannel pattern. In Step 4, a high-power ultrasonic cleanser was employed to remove the LTP product and light-absorbing layer from the surface of the PDMS substrate. In Step 5, a photomask prepared from polyimide (PI) was placed over the PDMS film, covering areas both with and without the microchannel array. Then, magnetron sputtering equipment was used to deposit an Au film on the exposed areas of the photomask. In Step 6, the PDMS film with microchannel arrays and a gold coating was segmented and packaged using liquid metal and shrinkable tubes.

The sensor was in the shape of a long strip, and the metal film on its surface was in the shape of a dumbbell. The sensing area of the metal layer in the center of the sensor was rectangular (30 × 5 mm). Meanwhile, the microchannel repeat intervals were set to 200, 600, and 1000 μm, respectively. Considering that the width of the microchannel was stabilized at 60 μm, the corresponding gaps between the microchannels were 140, 540, and 940 μm.

B. Materials and Equipment

During the experimental process, all chemicals were obtained from commercial sources and used without further purification. PDMS (Sylgard 184) was purchased from Dow Corning. The film ink type was chosen as Epson BK-T8231. Polyvinyl pyrrolidone [PVP, $(C_6H_9NO)_n$, Mw = 220 000] and anhydrous ethanol (CH_3CH_2OH, 99.5%) were procured from Shanghai Macklin Biochemical Company Ltd. The liquid metal (metal basis: 99.99% Ga–In–Sn) and single-sided conductive tape (3M7766-50) used in the packaging process were procured from Alfa Aesar Chemical Company Ltd. and 3M Company, respectively.

The PDMS with microchannel arrays was fabricated using an UV pulsed laser system (Grace X 355-3A, Han's Laser Technology Industry Group Company Ltd., wavelength: 355 nm). The laser scan speed was set at 10 mm/s,

and the motion in the X- and Y-direction was precisely controlled by software. The distance between the field lens and the sample was adjusted using the vertical Z-direction translation stage. To achieve LTP, the laser repetition frequency and laser power were set at 200 kHz and 1.8 W. The laser single pulse energy (E_{sp}) was calculated using the formula $E_{sp} = P_{avg}/f_{pr}$. The PDMS substrate patterned using LTP technology required further cleaning with an ultrasonic constant temperature cleaning machine (Ningbo Scientz Biotechnology Company Ltd., SBL-15DT). To effectively remove the pyrolysis products, the ultrasonic power was set to 480 W, and the cleaning time was set to 20 min. The deposition of the (Au) metal film on the PDMS surface was carried out using a magnetron sputtering coating machine (T-Z1650PVD, Zhengzhou Ketan Instrument Equipment Company Ltd.). The sputtering power was set at 55 W, the chamber was filled with argon (Ar) gas, and the vacuum level was maintained at 4 Pa. In the sensor packaging process, commercial single-sided conductive tapes were used as connecting wires. To ensure the reliability of the sensor during its application, liquid metal was coated onto these tapes. Subsequently, two heat-shrink tubes were heated at 130 °C for 20 s to protect and secure both ends of the sensor.

C. Characterization and Testing

The morphology of the PDMS substrate with microchannel arrays was characterized using a scanning electron microscope (SEM, Gemini 300, ZEISS) and a 3-D laser scanning microscope (VK-X1000, KEYENCE). The UV-visible (UV-Vis) is the absorption spectra of the light-absorbing coatings were characterized with a microvolume UV-V is spectrophotometer (NanoDrop[1] One, Thermo Fisher Scientific Inc.). The pyrolysis products were characterized with an X-ray diffraction (XRD) instrument (Rigaku Smartlab) at a scanning rate of 10 °C/min. The mechanical properties of the flexible strain sensor were assessed using a universal testing machine (TSE503A, Wance Testing Machine Company Ltd.). The corresponding electrical signals were captured with a data acquisition and logging system (DAQ6510, Keithley), and the response time was monitored with an oscilloscope (TBS2104B, Tektronix).

Flexible tensile strain sensors are widely used to measure minute physical deformations. Their sensitivity is typically evaluated using the GF, which is determined by the structure and material of the sensor. In the context of this study, the GF value of the resistance-based flexible strain sensor can be calculated using the formula: $GF = (\Delta R/R_0)/\varepsilon$. In this formula, ε represents strain, R_0 denotes the initial resistance of the sensor in its stable state, and ΔR is the change in resistance of the sensor due to external strain ε.

III. Results and Discussion

A. LTP Technology

It is well known that PDMS is a transparent polymer material that is used in numerous fields due to its excellent properties, such as flexibility, elasticity, and biocompatibility. To fabricate microstructures on the PDMS surface, a series of innovative fabrication technologies have been developed [33], [34]. Compared to the traditional template method, which has strict requirements for fabrication environments, equipment, and processes, laser direct pyrolysis technology stands out because of its efficiency, precision, controllability, and flexibility [35].

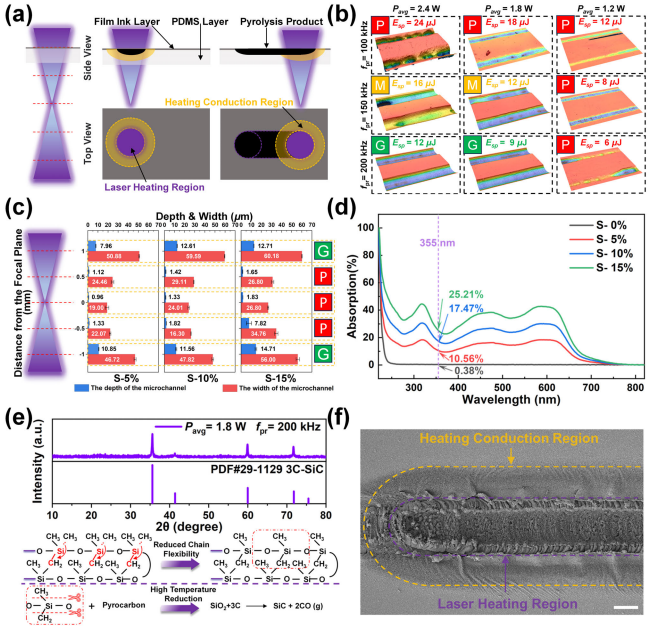

Fig. 2. (a) Schematic of the reaction mechanism of LTP. (b) Three-dimensional laser confocal images of PDMS microchannel morphology under different laser average powers and laser repetition frequencies (P, M, and G represent poor, medium, and good morphological quality, respectively). (c) Depth, width, and quality of the microchannel under different light-absorbing layers (wt%) and defocus distances (d_{def}). (d) UV-Vis absorption spectra of PVP absolute ethanol solutions with film inks of different mass percentages (0%, 5%, 10%, and 15%). (e) XRD pattern of products resulting from the LTP process, accompanied by a schematic of the reaction mechanism. (f) SEM image of PDMS surface after LTP reaction (scale bar: 20 μm).

Unlike the continuous laser pyrolysis described in our previous work [36], LTP ensures the continuity of the photothermal effect by introducing a semi-transparent light-absorbing layer. Specifically, as shown in Fig. 2(a), when the laser is vertically irradiated onto the light-absorbing layer covering the PDMS surface, most of the laser energy passes through the light-absorbing layer and PDMS substrate. Only a small portion of the energy is absorbed, leading to the formation of a laser heating region (LHR). Owing to the photothermal effect, the absorbed energy creates an ultrahigh-temperature gradient, subsequently triggering the laser pyrolysis reaction within the PDMS. Simultaneously, this process leads to the formation of a hemispherical pyrolysis product in the PDMS, facilitating heat transfer and forming a heat conduction region (HCR). Finally, the LTP reaction occurs iteratively as the laser moves.

On this basis, we investigated the effects of different laser average powers (P_{avg}) and pulse repetition frequencies (f_{pr}) on the morphology of the microchannels after LTP.

[1]Trademarked.

Correspondingly, Fig. 2(b) shows the 3-D laser confocal images of the PDMS microchannels after LTP treatment in the defocused state ($d_{def} = -1.0$ mm). Apparently, the LTP reaction achieved deeper microchannel depths under $P_{avg} = 2.4$ W and $f_{pr} = 100$ kHz ($E_{sp} = 24$ μJ). Correspondingly, owing to the strong photothermal effect, the sidewalls of the microchannels exhibited a relatively rough morphology. In contrast, under $P_{avg} = 1.2$ W and $f_{pr} = 150$ kHz ($E_{sp} = 6$ μJ), the intensity of the LTP reaction was notably weak, resulting in shallower microchannel depths and suboptimal morphology. Specifically, the single pulse energy determines the minimal threshold to initiate the LTP reaction. With adequate single pulse laser energy, the morphology of the microchannel is influenced by the synergistic effect of P_{avg} and f_{pr}. Considering the operation mechanism of pulsed lasers, it is found that lower P_{avg} in combination with higher f_{pr} produces a more optimal microchannel morphology. This is also the main criterion for selecting the process conditions ($P_{avg} = 1.8$ W and $f_{pr} = 200$ kHz) for the fabrication of the flexible strain sensors.

To investigate the effects of different light-absorbing layers (wt%) and defocus distances (d_{def}) on the microchannel fabrication, we analyzed the depth, width, and quality of the microchannels under different conditions, as shown in Fig. 2(c). The corresponding samples were labeled as S-5%, S-10%, and S-15%, respectively. We observed that as the mass percentage (wt%) of the film ink increased, the capacity of the light-absorbing layer to absorb UV laser increased, resulting in a corresponding increase in both the depth and width of the microchannels. This observation confirms that manipulating the light-absorbing layer can effectively control the reaction intensity of LTP. Interestingly, within the range of -0.5 and 0.5 mm around the focal plane, the quality of microchannels formed by the LTP reaction on the PDMS surface was poor. In contrast, optimal microchannel quality was realized at defocus distances farther from the focal plane ($d_{def} = -1$ and 1 mm). This observation further confirms that the LTP reaction near the focal plane is unstable due to factors, such as the accumulation and convergence of laser energy [37].

Correspondingly, Fig. 2(d) shows the UV-Vis light absorption spectra of PVP absolute ethanol solutions of film inks with different mass percentages (5, 10, and 15 wt%). It was evident that the absorption percentages of samples S-5%, S-10%, and S-15% at a wavelength of 355 nm were 10.56%, 17.47%, and 25.21%, respectively, showing clear differences. Meanwhile, we found that the uniformity of the light-absorbing layer on the PDMS surface was crucial for the morphology of the microchannels. This is also the primary reason for introducing the anhydrous ethanol solution of PVP as the dispersant and thickener of the film inks. Moreover, this approach effectively eliminates uncontrollable variables introduced by surface modification methods, such as UV or plasma treatment [38].

To explain the reaction mechanism of LTP further, we employed XRD to analyze the pyrolysis products, as shown in Fig. 2(e). The purple spectrum exhibited three main peaks at 35.6°, 60.0°, and 71.8°, unmistakably indicating the 3C-SiC products generated during the LTP reaction. In the specific reaction process, PDMS undergoes pyrolysis due to the laser energy absorbed by the light-absorbing layer, experiencing a high heating rate. In the initial stage of the LTP reaction, the high temperature induces the breaking and reforming of Si-CH_3 bonds on PDMS chains, thereby further enhancing the cross-linking of PDMS and generating silicon oxide and pyrolytic carbon on the PDMS surface. With increasing temperature, the silicon oxides in PDMS are directly reduced to 3C-SiC by the pyrolytic carbon in an oxygen-deficient environment [39].

Fig. 2(f) shows the SEM image of the PDMS surface after the LTP reaction. The morphology of the sample distinctly delineated both the laser heating and HCRs. Within the LHR, porous pyrolysis products (3C-SiC) were clearly observed. Meanwhile, at the edge of the LHR, a clear boundary existed between the pyrolysis products and the light-absorbing layer. This indicates that the light-absorbing layer, besides inducing the LTP reaction, does not further exacerbate the spread of pyrolysis. Additionally, significant delamination was observed between the pyrolysis products and the PDMS substrate. This phenomenon is mainly attributed to the differences in the thermal expansion coefficients of the various materials.

B. Performance Test of the Strain Sensor

With a thorough understanding of the LTP mechanism, it is possible to create customized microchannel patterns of various shapes on the PDMS surface. The fabrication parameters selected for the flexible strain sensor in terms of the UV laser were as follows: laser average power (P_{avg}) of 1.2 W, laser repetition frequency (f_{pr}) of 100 kHz, and laser defocus distance (d_{def}) of 1.0 mm. Building on this foundation, we designed and fabricated flexible strain sensors with the microchannel array at different LTP scanning intervals. In addition, the influence of different metal film thicknesses on the surface of the microchannel array was explored by controlling the sputtering time.

As shown in Fig. 3(a), the intervals for LTP scanning, from top to bottom, before sensor packaging were individually set to 1000, 600, and 200 μm (labeled as I-1000, I-600, and I-200). Concurrently, the flat surface PDMS substrate served as a control group to validate the performance enhancement of the flexible strain sensor (labeled as I-Flat). From left to right, the magnetron sputtering deposition times for the samples were set as 10, 20, and 30 s (labeled as T-10, T-20, and T-30). Apparently, samples with shorter sputtering times exhibit noticeable translucency. As the sputtering time increases, the transparency diminishes, and the sample eventually becomes opaque. From the SEM image of the sample (I-200&T-20), the laser scanning intervals were 200 μm, which contained a microchannel with a size of 60 μm, maintaining good structural consistency. The tiny cracks observed on the (Au) metal films are attributed to thermal stresses caused by the heating process of ion evaporation before the SEM imaging.

The metal-sputtered (Au) samples with microchannel arrays were sliced into specific sizes (a length of 50 mm, width of 8.4 mm, and height of 1 mm) and subsequently packaged into individual flexible strain sensors (sensor effective area: length

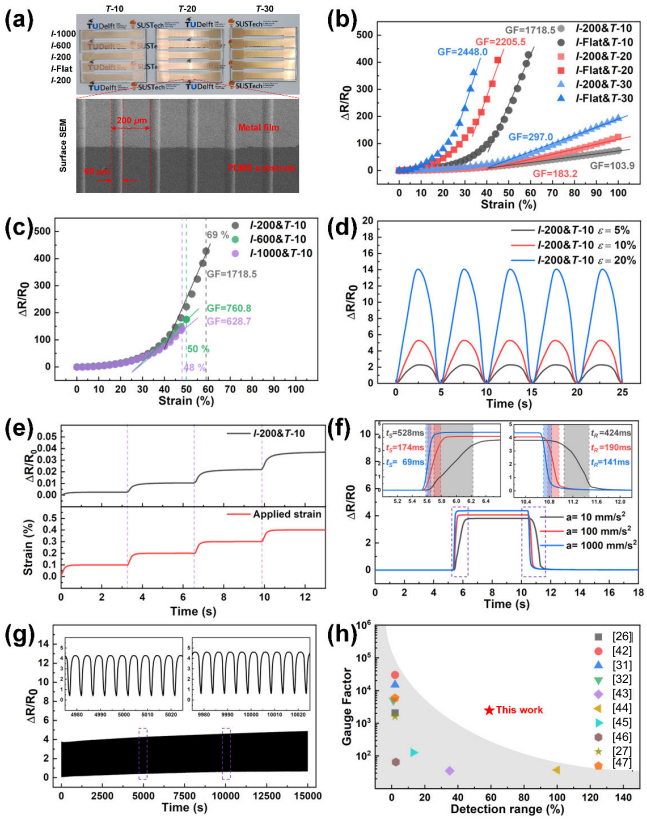

Fig. 3. (a) Optical images of different scanning intervals and Au sputtering times and the SEM image of local microchannel array. Relative resistance changes of strain sensors based on (b) different microchannel arrays and flat-surface under different strains and (c) different scanning intervals. Relative resistance response curve of the sensor under (d) large strain conditions (5%, 10%, and 20%) and (e) minor conditions (0.1%). (f) Response time and recovery time of the sensor under different stretch and release accelerations. (g) Relative resistance response curve of the sensor for 3000 stretch-release cycles at 10% strain. (h) Comparison of sensing range and GF with other reports.

30 mm and width 5 mm). The sensitivity and detection range of different sensors were evaluated as the vital performance indicators for flexible strain sensors. Fig. 3(b) shows the relative resistance changes ($\Delta R/R_0$) of different flexible strain sensors, with the microchannel array and the flat surface, under various strains (ε) during the stretching process. Compared to the flexible strain sensor with a flat surface, the introduction of microchannels significantly enhances the sensitivity of the flexible strain sensor. Taking the I-Flat&T-10 and I-200&T-10 sensors as typical examples, on the flat-surface PDMS substrate, after 10 s of metal sputtering, the GF value of the sensor (I-Flat&T-10) reached 103.9 after linear fitting within the 40%–100% strain range. Notedly, after introducing the microchannel array (channel width = 60 μm and scanning interval = 200 μm), the GF value of the sensor (I-200&T-10) increased to an ultrahigh 1718.5, with the performance increased by nearly 16 times. Correspondingly, due to the tradeoff relationship between sensitivity and detection range, the inherent detection range of the strain sensor with the microchannel array decreased to 69%. Furthermore, for the flexible strain sensors based on metal cracks, the thickness

TABLE I
SENSING PERFORMANCE OF FLEXIBLE STRAIN SENSORS

Sensor Type	Detection Range (ε)	Fitting Interval (ε)	Gauge Factor (GF)	Linearity (R^2)
I-200&T-10	0-59%	40-59%	1718.5	0.98
I-NLT&T-10	0-100%	40-100%	103.9	0.99
I-200&T-20	0-45%	35-45%	2205.5	0.98
I-NLT&T-20	0-100%	40-100%	183.2	0.99
I-200&T-30	0-34%	25-34%	2448.0	0.98
I-NLT&T-30	0-100%	29-100%	297.0	0.99

of the metal sputtering significantly affects their performance [16]. Evidently, as the metal sputtering time increased from 10 to 20 s and then to 30 s, the GF value of sensors with a flat surface rose from 103.9 to 183.2, finally reaching 297.0. Concurrently, the GF value of sensors with the microchannel array also climbed from 1718.0 to 2205.5 and further to 2448.0, while their detection range decreased from 59% to 45% and finally to 34%. Additionally, the performance of flexible strain sensors with different scanning intervals is shown in Fig. 3(c). It can be clearly observed that as the laser scanning interval increased from 200 to 600 μm and subsequently to 1000 μm, the GF value of the sensor dropped from 1718.5 to 760.8 and further down to 628.7. Meanwhile, the detection range of the sensor also diminished from 69% to 50% and then down to 48%. The detailed sensing performances of various sensor types are outlined in Table I. Importantly, the detection range limit for the sensors with the flat surface was set at 100% and not the limit of its detection range.

Among them, the device I-200&T-10 stood out with its extensive detection range coupled with exceptional sensitivity. Therefore, it was selected to further evaluate the performance of the flexible strain sensor. As shown in Fig. 3(d), when subjected to strains of 5%, 10%, and 20%, the sensor consistently showed a clear and stable response to five consecutive triangle wave strains, operating at a steady frequency of 0.2 Hz. Clearly, the sensor has a distinct response to large strains. As illustrated in Fig. 3(e), when subjected to four successive minor strains of 0.1%, its relative resistance change was in good agreement with the externally applied strain. Impressively, the sensor has a remarkably precise strain resolution.

To verify the response speed of the sensor, we measured its response time (stretch time, t_S) and recovery time (release time, t_R) under different stretch and release accelerations (10, 100, and 1000 mm/s^2). As shown in Fig. 3(f), with the increase in stretch and release acceleration, both the response and recovery times decreased significantly. It is worth noting that in all stretching and releasing accelerations, the recovery time is always slower than the response time, which is attributed to the intrinsic viscoelasticity of the PDMS material [40]. Specifically, at the maximum acceleration, the response and recovery times were 69 and 141 ms, respectively. These times are consistent with the requirements of flexible strain sensors for various applications [4]. The response and recovery

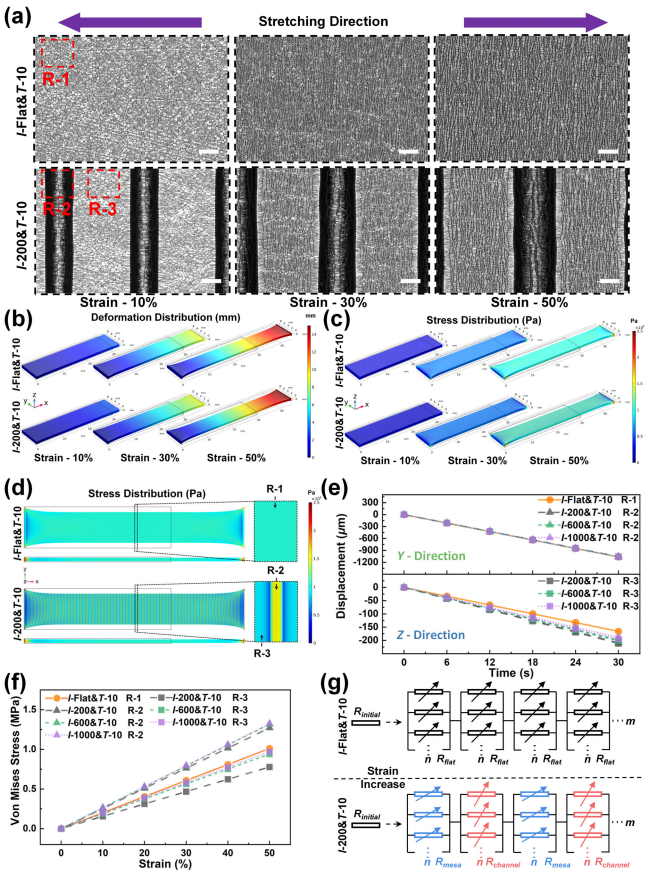

Fig. 4. (a) OM images of surface Au microcracks distribution of *I*-Flat&*T*-10 and *I*-200&*T*-10 under 10%, 30%, and 50% tensile strain conditions (scale bar: 50 μm). (b) and (c) Deformation and strain distribution of PDMS substrates with the flat surface and the microchannel array under different strain conditions (10%, 30%, and 50%). (d) Strain distribution of PDMS substrates with smooth surface and microchannel array under 50% strain state. (e) and (f) Changing trends of deformation and stress with different strains in different regions of PDMS substrates with smooth surfaces and microchannel arrays, respectively. (g) Equivalent circuit diagrams corresponding to PDMS substrates with the flat surface and the microchannel array.

times were defined as the time corresponding to the relative resistance change of the sensor from 10% to 90% [41].

To evaluate the long-term reliability of the flexible strain sensor, a constant strain of 10% was applied to the sensor over 3000 cycles at a 0.2-Hz frequency. As shown in Fig. 3(g), despite slight degradation during the stretching and releasing phases, the sensor with the microchannel array demonstrated remarkable long-term reliability without any significant failures.

As summarized in Fig. 3(h), the development of crack-based flexible strain sensors with high sensitivity and wide detection range is still challenging [26], [27], [31], [32], [42], [43], [44], [45], [46], [47]. However, utilizing LTP technology to design a flexible strain sensor with a microchannel array based on Au metal cracks is expected to provide a comprehensive solution to this challenge.

C. Mechanism Analysis of the Strain Sensor

To investigate the sensing mechanism, we conducted a systematic analysis comparing the distribution of Au cracks under different strain conditions between the sensor with the flat surface and the sensor with the microchannel array. Fig. 4(a) shows the optical microscopy (OM) images of *I*-Flat&*T*-10 and *I*-200&*T*-10 under the tensile strain conditions of 10%, 30%, and 50%. Under external strain, the surface Au film of the sensor developed elongated and random cracks perpendicular to the stretching direction. This crack propagation trend is consistent with previously reported studies on strain sensors based on metallic cracks [26], [31]. Specifically, for the *I*-Flat&*T*-10 sensor, the crack density was significantly lower under a 10% strain condition. In the flat region (R-1) of the PDMS substrate, surface stress induced fractures in the adhering Au film, resulting in crack formation and the release of energy from stretching [4]. As the strain increased to 30%, the number of cracks on the Au film rose noticeably, leading to a significant increase in microcrack density. At a strain of 50%, the microcrack density of the Au film reached saturation, and the microcrack spacing further expanded. In comparison, for the *I*-200&*T*-10 sensor, the crack propagation models of the Au film in the channel and mesa regions (R-2 and R-3) of the PDMS substrate exhibited distinct differences. Under 10% strain, the Au cracks in the mesa region (R-3) were basically consistent with the flat region of *I*-Flat&*T*-10. However, the Au cracks in the channel region (R-2) showed a lower crack density and a higher crack spacing. Similarly, as the strain increased to 30%, the crack density in the mesa region further increased. Notably, the crack density in the channel region remained largely stable, but the crack spacing further expanded. Under a strain of 50%, the crack densities in both the mesa and channel regions reached a steady state. However, with increasing external stretching, the crack spacing in the channel region expanded significantly. This is also the primary reason for the significant change in the relative resistance of the flexible strain sensor with microchannel arrays.

In fact, the primary cause of crack formation is the difference in elastic modulus between the PDMS substrate (0.5–3 MPa) and the Au film (27–37 GPa) [48], [49]. Specifically, the inherent flexibility of PDMS reduces its ability to constrain the deformation of the Au film. Consequently, when the sensor is subjected to external strain, the Au film undergoes localized deformation or necking, leading to the generation of cracks. To further investigate the effect of the microchannel array on the crack generation mechanism during the stretching of flexible sensors, we employed the finite element method (FEM) to simulate the deformation and strain distribution in the PDMS substrate [50]. Fig. 4(b) and (c) shows the deformation and strain distributions of the PDMS substrates with the flat surface and the microchannel array under different strain conditions (10%, 30%, and 50%). Based on the simulation results, the PDMS substrates with the flat surface and the microchannel array (*I*-Flat&*T*-10 and *I*-200&*T*-10) exhibited uniform deformation in the primary regions under different tensile strains. However, owing to the Poisson ratio of the PDMS material, a contraction occurred perpendicular to the stretch direction. This leads to an evident dumbbell-shaped morphology, particularly under large strain conditions (50%), potentially compromising the reliability of

the strain sensor. Meanwhile, for the stress distribution, PDMS substrates with the flat surface and the microchannel array (I-Flat&T-10 and I-200&T-10) exhibited consistent stress distribution under the small strain conditions (10%), with a negligible difference. Nevertheless, as the strain increased to 30% and 50%, both substrates revealed stress concentrations at their fixed boundaries. In contrast, the primary regions of the substrates sustained a relatively uniform and periodic stress distribution. Notably, under a large strain of 50%, the channel region (R-2) of the PDMS substrate with the microchannel arrays exhibited significantly higher stress compared to the adjacent mesa region (R-3), as shown in Fig. 4(d).

To systematically analyze the changing trends, we evaluated the maximum deformation and average stress distribution in different regions (R-1, R-2, and R-3) under different tensile strain conditions for all types of PDMS substrates, as shown in Fig. 4(e) and (f). In the Y-direction, the maximum surface deformation of different PDMS substrates remained relatively consistent. Conversely, in the Z-direction, PDMS substrates with low microchannel array density (I-1000&T-10) exhibited larger surface deformation as the strain increased. As the strain increased, the average surface stress in different regions of the PDMS substrates increased linearly. In PDMS substrates with microchannel arrays, the average surface stress in channel regions (R-2) was significantly higher than that in mesa regions (R-3). Meanwhile, for PDMS substrates with the flat surface, the average surface stress in the flat regions remained in an intermediate position. The abovementioned deformation and stress distributions are in good agreement with the Au crack morphology as well as the measured performances of the sensors. Higher stress leads to significant changes in the relative resistance of the sensor, further proving that the introduction of microchannels improves the sensitivity of metal crack-based strain sensors. However, this stress redistribution strategy still cannot break the tradeoff relationship between sensor sensitivity and detection range. In addition, a longer metal sputtering time will cause Au cracks on the surface of the sensor to more easily reach the fracture limit during the stretching process, resulting in a narrowing of the detection range. Counterintuitively, the lower the microchannel density, the higher the average surface stress in the channel area, which makes it easier for the Au cracks on the surface to reach the fracture limit, thus reducing the detection range of the sensor.

According to the conductive grid formed by the propagation of metal cracks, we define the sensor as a resistor network composed of m columns, each consisting of n resistors in parallel. Therefore, the total resistance of the sensor with a flat surface (R_{FS}) can be defined as

$$R_{\mathrm{FS}} = \frac{m}{n} R_{\mathrm{flat}} \tag{1}$$

where R_{falt} represents the crack gap resistance of the sensor with the flat surface. Correspondingly, the total resistance of the flexible strain sensor with a microchannel array (R_{MA}) is defined as

$$R_{\mathrm{MA}} = \frac{m}{2n}(R_{\mathrm{channel}} + R_{\mathrm{mesa}}) \tag{2}$$

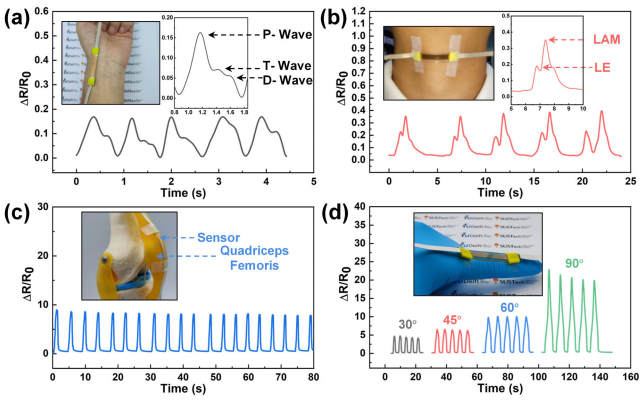

Fig. 5. (a) Relative resistance responses of the flexible strain sensor for monitoring pulse beats. Relative resistance responses of the sensor for (b) detecting pharyngeal swallowing, (c) monitoring knee flexion, and (d) detecting different finger bending angles (30°, 45°, 60°, and 90°).

where R_{channel} and R_{mesa} indicate the crack gap resistance of the sensor with the microchannel array, respectively.

The corresponding equivalent circuit diagrams are shown in Fig. 4(g). For sensors with a flat surface, under minor strain, crack generation is the dominant process, leading to increases in both m and n in the resistor network. During this stage (crack generation stage), since the crack growth direction is perpendicular to the tensile direction, m increases at a much faster rate than n. However, as the strain further increases, crack expansion becomes the dominant process, and both m and n in the resistor network reach saturation. During this stage (crack expansion stage), the expanding crack spacing causes a significant increase in the crack gap resistance (R_{flat}) in the network, becoming the main factor affecting the relative resistance change. For sensors with the microchannel array, the introduction of the microchannel array effectively redistributes the stress distribution on the PDMS surface, resulting in different crack propagation models. The stress is significantly more concentrated in the microchannel region compared to the mesa region. Under the same strain conditions, the crack density in the microchannel region saturates more quickly. As the strain increases further, the crack gap resistance in the channel region (R_{channel}) exceeds that in the mesa region (R_{mesa}). Although the sensor with the microchannel array has lower crack density when saturated compared to the sensor with the flat surface, the notable change in relative resistance due to crack spacing leads to greater sensitivity.

Overall, the above simulation results are in good agreement with the measurement and characterization results. The introduction of the microchannel array plays a vital role in the strain redistribution strategy, which significantly enhances the sensitivity of strain sensors based on metal cracks.

D. Practical Applications of the Strain Sensor

Benefiting from the high sensitivity and wide detection range of the designed flexible strain sensor, we extensively explored its capability to monitor signals for potential applications in health monitoring, human motion detection, and postoperative rehabilitation tracking.

For monitoring subtle physiological signals, pulse signals serve as effective indicators of heart function and blood circulation, playing a crucial role in the prevention, diagnosis, and management of cardiovascular conditions. As shown in Fig. 5(a), the flexible strain sensor was affixed to the radial artery side of the wrist, capturing the slight strain of the skin induced by pulse beats. Under standard conditions, the sensor identified the typical wrist pulse curve, where its relative resistance change exhibited periodic fluctuations and clear peaks synchronized with each heartbeat. The magnified relative resistance responses distinctly revealed the percussion wave, tidal wave, and diastolic waves (P-wave, T-wave, and D-wave) characteristic of the human pulse. Moreover, monitoring the swallowing process is essential for assessing swallowing disorders and valuable for daily observations of abnormal behaviors. As shown in Fig. 5(b), the flexible sensor was attached to the throat to detect the subtle strains generated by the swallowing action. The relative resistance change of the sensor exhibited swift and periodic responses consistent with the swallowing action, generating a corresponding swallowing curve. This enlarged swallowing curve clearly illustrated the processes of larynx elevation (LE) and larynx anterior movement (LAM) during swallowing. These results further verify the potential application of the sensor in the field of small strain detection.

For large-scale motion signals, assessing the range of motion in the knee joint after total knee arthroplasty (TKA) is critical for postoperative rehabilitation tracking and recovery evaluation. As shown in Fig. 5(c), the flexible strain sensor was secured to the surface of the quadriceps muscle on a knee joint model, aiming to monitor the flexion of the knee joint. The relative resistance change consistently fluctuated during the continuous 45° bending motion, and notably, the sensor met a strain threshold of 50% [51]. Furthermore, the evaluations of finger bending serve as valuable tools for medical professionals, enabling them to accurately determine both the range of motion and the severity of impairment in patients with rheumatoid arthritis, osteoarthritis, or other forms of arthritis. As shown in Fig. 5(d), the flexible sensor was attached between the proximal and middle phalanges to detect finger bending. With increasing finger bending angles (30°, 45°, 60°, and 90°), the relative resistance change of the sensor exhibited significant proportional changes. These results further demonstrate the potential application of the sensor in the field of large strain detection.

IV. Conclusion

In summary, we have successfully developed a flexible strain sensor based on gold (Au) cracks with a microchannel array fabricated by LTP technology. Through extensive experiments, we have revealed its operating conditions and pyrolysis mechanism. Using this technology, we have achieved a surface stress redistribution strategy for microchannel arrays on PDMS surfaces, resulting in a dramatic increase in the sensitivity of sensors with microchannel arrays compared to conventional flat surface sensors. The sensor exhibited high sensitivity (GF = 2448), excellent strain resolution (0.1%), wide detection range (59%), fast response and recovery times (69 and 141 ms, respectively), and robust durability (over 3000 cycles). Notably, the sensor could not only precisely detect subtle physiological signals, such as pulse and swallowing, but also monitor large-scale motion signals, such as knee flexion and finger bending. This study provides a promising technology platform for designing and fabricating high-performance flexible strain sensors based on metal cracks and opens up vast possibilities for their application in the field of health monitoring, human–machine interactions, and electronic skin.

Acknowledgment

The authors would like to express their deepest gratitude to Shenzhen Yixin Information Technology Company Ltd., Shenzhen, China. Their unwavering support, technical expertise, and dedication played an integral role in the success of our project.

References

[1] J. Huang et al., "Wrinkle-enabled highly stretchable strain sensors for wide-range health monitoring with a big data cloud platform," *ACS Appl. Mater. Interfaces*, vol. 12, no. 38, pp. 43009–43017, Sep. 2020.

[2] H. Zhang et al., "A flexible wearable strain sensor for human-motion detection and a human–machine interface," *J. Mater. Chem. C*, vol. 10, no. 41, pp. 15554–15564, 2022.

[3] J. Zhou et al., "Highly sensitive and stretchable strain sensors based on serpentine-shaped composite films for flexible electronic skin applications," *Compos. Sci. Technol.*, vol. 197, Sep. 2020, Art. no. 108215.

[4] M. Amjadi, K. Kyung, I. Park, and M. Sitti, "Stretchable, skin-mountable, and wearable strain sensors and their potential applications: A review," *Adv. Funct. Mater.*, vol. 26, no. 11, pp. 1678–1698, Mar. 2016.

[5] H. Cai et al., "Trehalose-enhanced ionic conductive hydrogels with extreme stretchability, self-adhesive and anti-freezing abilities for both flexible strain sensor and all-solid-state supercapacitor," *Chem. Eng. J.*, vol. 472, Sep. 2023, Art. no. 144849.

[6] H. Xu, Y. Lv, D. Qiu, Y. Zhou, H. Zeng, and Y. Chu, "An ultra-stretchable, highly sensitive and biocompatible capacitive strain sensor from an ionic nanocomposite for on-skin monitoring," *Nanoscale*, vol. 11, no. 4, pp. 1570–1578, 2019.

[7] M. Bobinger et al., "Light and pressure sensors based on PVDF with sprayed and transparent electrodes for self-powered wireless sensor nodes," *IEEE Sensors J.*, vol. 19, no. 3, pp. 1114–1126, Feb. 2019.

[8] J. Liu, L. Zhang, N. Wang, and C. Li, "Highly stretchable and transparent triboelectric nanogenerator based on multilayer structured stable electrode for self-powered wearable sensor," *Nano Energy*, vol. 78, Dec. 2020, Art. no. 105385.

[9] A. S. Fiorillo, C. D. Critello, and S. A. Pullano, "Theory, technology and applications of piezoresistive sensors: A review," *Sens. Actuators A, Phys.*, vol. 281, pp. 156–175, Oct. 2018.

[10] A. A. Barlian, W.-T. Park, J. R. Mallon, A. J. Rastegar, and B. L. Pruitt, "Semiconductor piezoresistance for microsystems," *Proc. IEEE*, vol. 97, no. 3, pp. 513–552, Mar. 2009.

[11] Z. Duan et al., "Inspiration from daily goods: A low-cost, facilely fabricated, and environment-friendly strain sensor based on common carbon ink and elastic core-spun yarn," *ACS Sustain. Chem. Eng.*, vol. 7, no. 20, pp. 17474–17481, Oct. 2019.

[12] J. Chen, Y. Zhu, and W. Jiang, "A stretchable and transparent strain sensor based on sandwich-like PDMS/CNTs/PDMS composite containing an ultrathin conductive CNT layer," *Compos. Sci. Technol.*, vol. 186, Jan. 2020, Art. no. 107938.

[13] J. Lee et al., "A stretchable strain sensor based on a metal nanoparticle thin film for human motion detection," *Nanoscale*, vol. 6, no. 20, pp. 11932–11939, 2014.

[14] M.-S. Lee et al., "High-performance, transparent, and stretchable electrodes using graphene-metal nanowire hybrid structures," *Nano Lett.*, vol. 13, no. 6, pp. 2814–2821, May 2013.

[15] J. Kim, S. W. Lee, M. H. Kim, and O. O. Park, "Zigzag-shaped silver nanoplates: Synthesis via Ostwald ripening and their application in highly sensitive strain sensors," *ACS Appl. Mater. Interfaces*, vol. 10, no. 45, pp. 39134–39143, Nov. 2018.

[16] R. Zhou et al., "Hierarchical synergistic structure for high resolution strain sensor with wide working range," *Small*, vol. 19, no. 34, Aug. 2023, Art. no. 2301544.

[17] Y.-C. Qiao et al., "Graphene devices based on laser scribing technology," *Jpn. J. Appl. Phys.*, vol. 57, no. 4, Apr. 2018, Art. no. 04FA01.

[18] C. Yang, D. Zhang, D. Wang, H. Luan, X. Chen, and W. Yan, "In situ polymerized MXene/polypyrrole/hydroxyethyl cellulose-based flexible strain sensor enabled by machine learning for handwriting recognition," *ACS Appl. Mater. Interfaces*, vol. 15, no. 4, pp. 5811–5821, Feb. 2023.

[19] Y. Ma et al., "Self-adhesive, anti-freezing MXene-based hydrogel strain sensor for motion monitoring and handwriting recognition with deep learning," *ACS Appl. Mater. Interfaces*, vol. 15, no. 24, pp. 29413–29424, Jun. 2023.

[20] T. Li et al., "A flexible strain sensor based on CNTs/PDMS microspheres for human motion detection," *Sens. Actuators A, Phys.*, vol. 306, May 2020, Art. no. 111959.

[21] M. Li, S. Chen, B. Fan, B. Wu, and X. Guo, "Printed flexible strain sensor array for bendable interactive surface," *Adv. Funct. Mater.*, vol. 30, no. 34, Aug. 2020, Art. no. 2003214.

[22] Y. Li, T. He, L. Shi, R. Wang, and J. Sun, "Strain sensor with both a wide sensing range and high sensitivity based on braided graphene belts," *ACS Appl. Mater. Interfaces*, vol. 12, no. 15, pp. 17691–17698, Apr. 2020.

[23] S. Tadakaluru, W. Thongsuwan, and P. Singjai, "Stretchable and flexible high-strain sensors made using carbon nanotubes and graphite films on natural rubber," *Sensors*, vol. 14, no. 1, pp. 868–876, Jan. 2014.

[24] P. Costa, C. Silvia, J. C. Viana, and S. L. Mendez, "Extruded thermoplastic elastomers styrene-butadiene-styrene/carbon nanotubes composites for strain sensor applications," *Compos. B, Eng.*, vol. 57, pp. 242–249, Feb. 2014.

[25] X. Wu, Y. Han, X. Zhang, and C. Lu, "Highly sensitive, stretchable, and wash-durable strain sensor based on ultrathin conductive layer@ polyurethane yarn for tiny motion monitoring," *ACS Appl. Mater. Interfaces*, vol. 8, no. 15, pp. 9936–9945, Apr. 2016.

[26] D. Kang et al., "Ultrasensitive mechanical crack-based sensor inspired by the spider sensory system," *Nature*, vol. 516, no. 7530, pp. 222–226, Dec. 2014.

[27] T. Lee, Y. W. Choi, G. Lee, S. M. Kim, D. Kang, and M. Choi, "Crack-based strain sensor with diverse metal films by inserting an inter-layer," *RSC Adv.*, vol. 7, no. 55, pp. 34810–34815, 2017.

[28] D. Qi, K. Zhang, G. Tian, B. Jiang, and Y. Huang, "Stretchable electronics based on PDMS substrates," *Adv. Mater.*, vol. 33, no. 6, Feb. 2021, Art. no. 2003155.

[29] M. Amjadi, M. Turan, C. P. Clementson, and M. Sitti, "Parallel microcracks-based ultrasensitive and highly stretchable strain sensors," *ACS Appl. Mater. Interfaces*, vol. 8, no. 8, pp. 5618–5626, Mar. 2016.

[30] Z. Chu, W. Jiao, Y. Huang, Y. Zheng, R. Wang, and X. He, "Superhydrophobic gradient wrinkle strain sensor with ultra-high sensitivity and broad strain range for motion monitoring," *J. Mater. Chem. A*, vol. 9, no. 15, pp. 9634–9643, 2021.

[31] B. Park et al., "Dramatically enhanced mechanosensitivity and signal-to-noise ratio of nanoscale crack-based sensors: Effect of crack depth," *Adv. Mater.*, vol. 28, no. 37, pp. 8130–8137, Oct. 2016.

[32] T. Yang et al., "Structural engineering of gold thin films with channel cracks for ultrasensitive strain sensing," *Mater. Horizons*, vol. 3, no. 3, pp. 248–255, 2016.

[33] J. Shin et al., "Monolithic digital patterning of polydimethylsiloxane with successive laser pyrolysis," *Nature Mater.*, vol. 20, no. 1, pp. 100–107, Jan. 2021.

[34] Z. Ji, D. Jiang, X. Zhang, Y. Guo, and X. Wang, "Facile photo and thermal two-stage curing for high-performance 3D printing of poly(dimethylsiloxane)," *Macromolecular Rapid Commun.*, vol. 41, no. 10, May 2020, Art. no. 2000064.

[35] K. Min et al., "Fabrication of perforated PDMS microchannel by successive laser pyrolysis," *Materials*, vol. 14, no. 23, p. 7275, Nov. 2021.

[36] S. Wang et al., "Rapid fabrication of high-performance flexible pressure sensors using laser pyrolysis direct writing," *ACS Appl. Mater. Interfaces*, vol. 15, no. 34, pp. 41055–41066, Aug. 2023.

[37] T. A. Meinhold and N. Kumar, "Radiation pressure acceleration of protons from structured thin-foil targets," *J. Plasma Phys.*, vol. 87, no. 6, Dec. 2021, Art. no. 905870607.

[38] J. Zhu, X. Wu, J. Jan, S. Du, J. Evans, and A. C. Arias, "Tuning strain sensor performance via programmed thin-film crack evolution," *ACS Appl. Mater. Interfaces*, vol. 13, no. 32, pp. 38105–38113, Aug. 2021.

[39] G. Camino, S. M. Lomakin, and M. Lageard, "Thermal polydimethylsiloxane degradation—Part 2. The degradation mechanisms," *Polymer*, vol. 43, no. 7, pp. 2011–2015, Mar. 2002.

[40] E. K. Dimitriadis, F. Horkay, J. Maresca, B. Kachar, and R. S. Chadwick, "Determination of elastic moduli of thin layers of soft material using the atomic force microscope," *Biophys. J.*, vol. 82, no. 5, pp. 2798–2810, May 2002.

[41] Y. X. Song, W. M. Xu, M. Z. Rong, and M. Q. Zhang, "A sunlight self-healable transparent strain sensor with high sensitivity and durability based on a silver nanowire/polyurethane composite film," *J. Mater. Chem. A*, vol. 7, no. 5, pp. 2315–2325, 2019.

[42] T. Kim et al., "Spider-inspired tunable mechanosensor for biomedical applications," *npj Flexible Electron.*, vol. 7, no. 1, p. 12, Mar. 2023.

[43] Y. Hu et al., "Highly sensitive omnidirectional signal manipulation from a flexible anisotropic strain sensor based on aligned carbon hybrid nanofibers," *J. Mater. Chem. A*, vol. 10, no. 2, pp. 928–938, 2022.

[44] S. Zhu et al., "Inherently conductive poly(dimethylsiloxane) elastomers synergistically mediated by nanocellulose/carbon nanotube nanohybrids toward highly sensitive, stretchable, and durable strain sensors," *ACS Appl. Mater. Interfaces*, vol. 13, no. 49, pp. 59142–59153, Dec. 2021.

[45] D. Zhao et al., "Highly sensitive and flexible strain sensor based on AuNPs/CNTs' synergic conductive network," *Appl. Nanosci.*, vol. 9, no. 7, pp. 1469–1478, Oct. 2019.

[46] L. Zhao et al., "Laser-patterned hierarchical aligned micro-/nanowire network for highly sensitive multidimensional strain sensor," *ACS Appl. Mater. Interfaces*, vol. 14, no. 42, pp. 48276–48284, Oct. 2022.

[47] Z. Han et al., "High-performance flexible strain sensor with bio-inspired crack arrays," *Nanoscale*, vol. 10, no. 32, pp. 15178–15186, 2018.

[48] H. Cong and T. Pan, "Photopatternable conductive PDMS materials for microfabrication," *Adv. Funct. Mater.*, vol. 18, no. 13, pp. 1912–1921, Jul. 2008.

[49] C.-W. Baek, J.-M. Kim, Y.-K. Kim, J. H. Kim, H. J. Lee, and S. W. Han, "Mechanical characterization of gold thin films based on strip bending and nanoindentation test for MEMS/NEMS applications," *Sensors Mater.*, vol. 17, no. 5, pp. 277–288, Jan. 2005.

[50] G. Ding, S. Yue, S. Zhang, and W. Song, "Strain—Deformation reconstruction of CFRP laminates based on ko displacement theory," *Nondestruct. Test. Eval.*, vol. 36, no. 2, pp. 145–157, Mar. 2021.

[51] S. Li et al., "Contact-resistance-free stretchable strain sensors with high repeatability and linearity," *ACS Nano*, vol. 16, no. 1, pp. 541–553, Jan. 2022.